Exciton spectra and layer decomposition in math xmlns="http://www.w3.org/1998/Math/MathML">mrow>msub>mi>MoSi/mi>mn>2/mn>/msub>msub>mi mathvariant="normal">N/mi>mn>4/mn>/msub>mo>//mo>msub>mi>WSi/mi>mn>2/mn>/msub>msub>mi mathvariant="normal">N/mi>mn>4/mn>/msub>/mrow>/math> heterostructures

Hongxia Zhong, Shiyuan Gao, Guangyong Zhang, Zhengyu Xu, Jianmeng Zhou, Xingbing Li, Cheng Lu, and Yunhua Wang

Phys. Rev. B **108**, 205131 — Published 15 November 2023

DOI: 10.1103/PhysRevB.108.205131

Atypical exciton spectra and their macroscopic dielectric models in $MoSi_2N_4/WSi_2N_4$ heterostructures

Hongxia Zhong,[1] Shiyuan Gao,[2] Guangyong Zhang,[1] Zhengyu Xu,[1]
Jianmeng Zhou,[1] Xingbing Li,[1] Cheng Lu,[1] and Yunhua Wang[3,*]

[1] *School of Mathematics and Physics, China University of Geosciences, Wuhan 430074, China*
[2] *Institute for Quantum Matter and Department of Physics and Astronomy, Johns Hopkins University, Baltimore, Maryland 21218, USA*
[3] *Lanzhou Center of Theoretical Physics & Key Laboratory for Quantum Theory and Applications of the Ministry of Education & Key Laboratory of Theoretical Physics of Gansu Province & School of Physical Science and Technology, Lanzhou University, Lanzhou 730000, China*

Excitons in van der Waals heterostructures having interlayer or intralayer types are responsible for their optical absorption properties. Here, we systematically investigate the band alignment and excitons in $MoSi_2N_4/WSi_2N_4$ heterostructure using ab initio GW calculations and Bethe-Salpeter equation. The quasiparticle energy spectrum shows that the valence band maximum and conduction band minimum are from different layers, and hence the band alignment is type II in this heterostructure. However, unlike normal type-II heterostructures with interlayer excitons at the lowest energy, $MoSi_2N_4/WSi_2N_4$ heterostructure behaves like a type-I heterostructure, in which the optical excitation at the lowest energy is the intralayer exciton while the interlayer exciton is higher in energy. We develop a macroscopic dielectric model explaining the atypical exciton feature as a result of the large layer distance and the small exciton Bohr radius in this heterostructure. In addition, we find that the interlayer exciton is dark due to the absence of band hybridizations between the two layers, and the energy and oscillator strength of intralayer exciton are almost independent of the stacking configuration. These new results enrich the exciton mechanism in 2D layer materials and are beneficial for the design of optoelectronic devices based on moiré heterostructures.

I. INTRODUCTION

Stacking two monolayers together forms van der Waals (vdW) heterostructures, which not only inherit the original properties of monolayers but also induce new physical features. The type-II vdW heterostructures (i.e., the valence band maximum and conduction band minimum contributed by different layers) enable the formation of interlayer excitons. Such bound interlayer electron-hole pairs with the charges residing in different layers have ultralong lifetime and thus form an ideal platform for realizing bosonic many-particle states such as Bose-Einstein condensates[1, 2]. Owing to the type-II band alignments from different layers, the interlayer exciton usually lies at the lowest energy in transition metal dichalcogenide heterostructures[3, 4]. Two monolayers with different orientations (i.e., with a twist angle) form a moiré superlattice with a relatively large period, which can be viewed as regions with high-symmetry stacking separated by domain walls[5], giving rise to an exciton lattice centered on high-symmetry stacking regions[6, 7]. It has been demonstrated that the periodic moiré pattern can significantly modulate the electronic band structure and induce multiple interlayer exciton resonances in experiments[8]. Therefore, the moiré pattern in two-dimensional semiconductors is a novel platform for engineering new types of excitons and realizing their applications in optoelectronics.

Recently, monolayer $MoSi_2N_4$, a new member of the family of 2D molybdenum nitrides without bulk phases, has been synthesized by chemical vapor deposition[9]. Along the z direction, it has a septuple atomic layer with 1.17 nm thickness, which can be viewed as a MoN_2 layer passivated by two Si-N bilayers, leading to the ambient stability of $MoSi_2N_4$ monolayers[9]. The excellent mechanical properties and ambient stability of monolayer $MoSi_2N_4$ have stimulated several investigations on its physical properties such as spin-valley coupling[10–12], high thermal conductivity[13] and piezoelectricity[14]. However, only two works are performed on the excitonic properties of $MoSi_2N_4$[15, 16], especially for the exciton absorptions in monolayer and bilayer $MoSi_2N_4$ and their response to the in-plane strain[15, 16]. However, the interlayer excitons and their theoretical mechanisms in molybdenum nitride heterostructures have not been investigated yet. This work aims to reveal the formation of different types of excitons and their spectral features in $MoSi_2N_4/WSi_2N_4$ heterostructure, and meanwhile, develop the corresponding macroscopic dielectric model.

We use first-principles GW-Bethe Salpeter equation (BSE) approach to systematically calculate the quasiparticle band structure, the optical absorption spectra and the formation and properties of different types of excitons in $MoSi_2N_4/WSi_2N_4$ heterostructure. The calculated results show that the energy of interlayer excitons is higher than that of intralayer excitons in this heterostructure, which is strikingly different from the behavior of interlayer excitons always as the lowest excitations in usual transition metal dichalcogenide heterostructures[3, 4]. This atypical behavior of interlayer excitons is attributed

* wangyunhua@lzu.edu.cn

to the large layer distance and small exciton Bohr radius in $MoSi_2N_4/WSi_2N_4$ heterostructure from our constructed macroscopic dielectric model. For the intralayer excitons, the energy and optical dipole oscillator strength are almost independent of the stacking configuration. The atypical interlayer exciton and robust intralayer exciton in type-II $MoSi_2N_4/WSi_2N_4$ heterostructures enrich the present excitonic properties in vdW heterostructures and will further stimulate more experimental works and applications towards optoelectronics in molybdenum nitrides based vdW heterostructures.

II. COMPUTATIONAL DETAILS

We fully relax $MoSi_2N_4/WSi_2N_4$ heterostructure according to the force and stress calculated by density functional theory (DFT) with the Perdew, Burke, and Ernzerhof (PBE) functional[17], using the QUANTUM ESPRESSO package[18]. The van der Waals corrections (vdW-DF) are utilized to include the interlayer interaction[19]. The ground state wave functions and eigenvalues are obtained from the DFT/PBE with norm-conserving pseudopotentials which include the semi-core states of transition metal M[20]. The plane-wave basis is set with a cutoff energy of 80 Ry with a 16 × 16 × 1 k-point grid. The total energy is converged to less than 10^{-6} eV, and the maximum force is less than 0.01 eV/Å. A vacuum space between neighboring layers is set to be more than 25 Å to avoid interactions between adjacent layers. Based on these parameters, the relaxed lattice constant for monolayer $MoSi_2N_4$ (WSi_2N_4) is 2.910 Å (2.912 Å), agreeing well with previous calculations[9, 21] and leading to nearly zero lattice mismatch in $MoSi_2N_4/WSi_2N_4$ heterostructure.

The excited-state properties of the heterostructure are calculated by the GW approximation within the general plasmon pole model[22], which is reliable in obtaining the excitonic properties of 2D materials. The unoccupied conduction band number involved in calculating the dielectric function, self-energy, and absolute band edge is set to be 2000 after converge test. The 24 × 24 × 1 coarse k grid is used in calculating GW quasiparticle band gaps and the coarse-grid e-h interaction kernel. In solving the BSE, we use a finer k-point grid of 48 × 48 × 1 for converged excitonic states. We note that a marginal error of 0.1-0.2 eV could still be present in the exciton binding energy due to the slow convergence of GW+BSE calculation with respect to k-point grid in low-dimensional systems[23, 24]. All the GW-BSE calculations are performed with the BerkeleyGW code[25, 26] including the slab Coulomb truncation scheme to mimic interactions between structures[27, 28]. For optical absorption spectra, only the incident light polarized parallel with the plane is considered due to the depolarization effect[29, 30].

III. QUASIPARTICLE ELECTRONIC STRUCTURES IN AA-STACKED $MOSI_2N_4/WSI_2N_4$ HETEROSTRUCTURE

Let us first study quasiparticle electronic structures of AA-stacked $MoSi_2N_4/WSi_2N_4$ heterostructure, where the Mo (Si, N) atoms in one layer fully overlap with the W (Si, N) atoms in the WSi_2N_4 layer. The optimized layer distance between Mo and W atom is 10.492 Å, much larger than that (6.23–6.54 Å) of bilayer TMDCs, such as MoS_2 and WS_2[31, 32]. This suggests that, compared with bilayer TMDCs, the interlayer vdW interaction in $MoSi_2N_4/WSi_2N_4$ heterostructure is much weaker, which is a result of the two passivated SiN_2 pyramid layers and has been observed in bilayer $MoSi_2N_4$[33]. Such weak interlayer interaction indicates quite weak band hybridization between the two layers in the band edge of $MoSi_2N_4/WSi_2N_4$ heterostructure, as shown in Fig. 1(a). This is different from bilayer or bulk TMDCs, where the obvious hybridization of chalcogen p-states at the Γ point results in the crossover from direct band gaps in monolayers to indirect band gaps in multilayers[34]. In detail, the VBM and CBM of $MoSi_2N_4/WSi_2N_4$ heterostructure are contributed by WSi_2N_4 and $MoSi_2N_4$ layer, respectively, indicating the type-II heterostructure. The VBM is dominated by W d_{z^2} and $d_{x^2-y^2}$ orbitals, while CBM mainly consists of Mo d_{z^2} orbitals, accompanied by N p orbitals. On the whole, it is clearly shown that the indirect band gap feature and band dispersion of monolayer $MoSi_2N_4$ are almost unaffected by the WSi_2N_4 substrate, and vice versa. Therefore, the effect of wavefunction overlap might be ignored in MA_2Z_4-based heterostructures.

Fig. 1(b) shows the absolute band edge energies of monolayer $MoSi_2N_4$ (WSi_2N_4) in $MoSi_2N_4/WSi_2N_4$ heterostructure. The values of VBM and CBM in $MoSi_2N_4$ are lower than those of WSi_2N_4, confirming the type-II band alignment of $MoSi_2N_4/WSi_2N_4$ heterostructure, which is consistent with the projected band structure analysis in Fig. 1(a). At the DFT level, the absolute VBM and CBM of monolayer $MoSi_2N_4$ (WSi_2N_4) in the contact system are very close to those of free-standing sample, with energy difference smaller than 0.05 eV. After including quasiparticle correction, compared with the suspended monolayer, the supported $MoSi_2N_4$ (WSi_2N_4) possesses almost the same CBM energy, while with higher VBM. The quasiparticle correction pushes up the VBM by 0.153 eV (0.051 eV) for supported MoS_2N4 (WSi_2N_4), leading to a 4.9% (1.7%) reduction in quasiparticle band gap compared to free-standing monolayers. Comparing the band edge energies at DFT and GW levels, we can conclude that this environment-induced renormalization of the quasiparticle band gaps is a result of many-body effects on the screening and thus not apparent at the DFT level. On the other hand, the renormalization of the quasiparticle band gap of supported $MoSi_2N_4$ is the same as the bilayer $MoSi_2N_4$[16], confirming the reliability of our results. This quasiparticle band gap renormalization

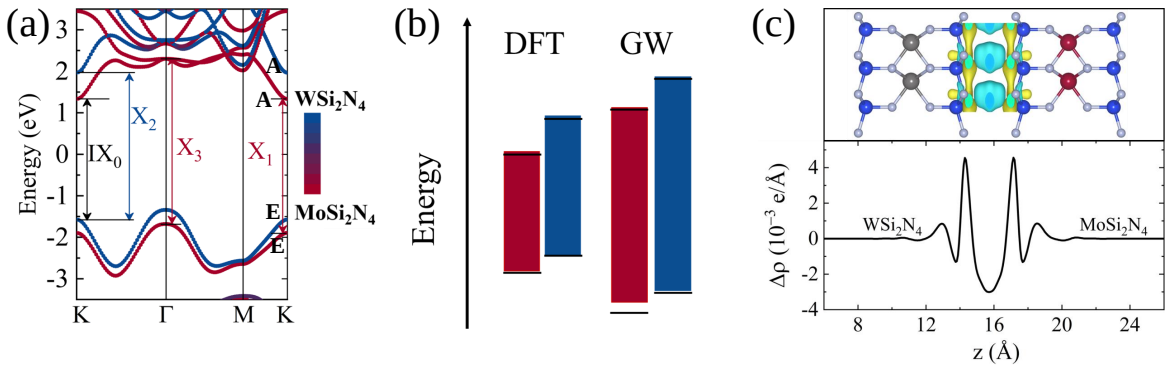

FIG. 1. The quasiparticle band structure of AA-stacked $MoSi_2N_4/WSi_2N_4$ heterostructure with the irreducible representations of energy bands at K point. IX_0, X_1, X_2, and X_3 label the intersubband transitions at K and Γ that give rise to the corresponding excitonic or interband-transition peaks in Fig. 3. (b) Band alignments of monolayer $MoSi_2N_4$ (WSi_2N_4) in AA-stacked $MoSi_2N_4/WSi_2N_4$ structure calculated by PBE and GW calculations, where the band alignments of suspended monolayers (black lines) are listed for comparison. The red and blue rectangles represent the band alignments of $MoSi_2N_4$ and WSi_2N_4, respectively. (c) Plane-averaged charge density difference $\Delta\rho(x)$ of $MoSi_2N_4/WSi_2N_4$ heterostructure. The top panel is a three-dimensional charge density difference, and the isosurface value is 2×10^{-5} e/Å^3. The yellow and blue areas represent electron accumulation and depletion, respectively.

is very small in comparison with those of encapsulated monolayer black phosphorus ($MoSe_2$), whose quasiparticle band gap is reduced by 25% (11%)[35, 36]. The small renormalization originates from the outer passivated Si-N bilayers in $MoSi_2N_4$ and WSi_2N_4, which protect the band edge states from the dielectric screening. In this sense, the absolute band edge energy of isolated monolayer MA_2Z_4 is still instructive for realistic conditions with surrounded dielectric environment.

Apart from dielectric screening, charge transfer could also affect the band alignment of $MoSi_2N_4/WSi_2N_4$ heterostructure. In order to quantify this effect, we extract the plane-averaged charge density difference $\Delta\rho(z)$ along the vertical direction (z axis) for $MoSi_2N_4/WSi_2N_4$ heterostructure in Fig. 1(c). Here, $\Delta\rho(z)$ is calculated by the charge density difference between the heterostructure and two noninteracting monolayers. For $MoSi_2N_4/WSi_2N_4$ heterostructure, the $\Delta\rho(z)$ is on the order of 10^{-3} e/Å, which is one order of magnitude smaller than that of typical type-II TMDC heterostructure like $PtS_2/MoTe_2$[37]. This suggests small charge transfer between layers, consistent with the observed very weak interlayer vdW interaction in $MoSi_2N_4/WSi_2N_4$ heterostructure. On the whole, we can see clearly that changes in $\Delta\rho(z)$ are almost symmetric on the two sides of the interface. This is very different from the asymmetric $\Delta\rho(z)$ for other bilayers such as strained bilayer $MoSi_2N_4$ and TMDC[33, 37]. This symmetric charge difference indicates that the charge transfer is very small in $MoSi_2N_4/WSi_2N_4$ heterostructure, leading to the weak interlayer interaction in MA_2Z_4. It is the negligible charge transfer between the sublayeres in MA_2Z_4 heterostructures that results in insignificant interlayer interaction for MA_2Z_4 bilayers.

IV. STACKING-INDEPENDENT EXCITONS IN $MOSI_2N_4/WSI_2N_4$ HETEROSTRUCTURE

In a real $MoSi_2N_4/WSi_2N_4$ heterostructure, two individual layers have different orientations, forming a twist angle and a moiré superlattice with a relatively large period. A small-angle moiré superlattice can be viewed as regions of high-symmetry stacking separated by domain walls[5], in which the periodic modulation of local potential give rise to an exciton lattice centered on high-symmetry stacking region forms[6, 7]. Hence, we will pay attention to specific stacking styles and calculate their local excitonic properties. As shown in Fig. 2, we take the R type as an example to study the twist-angle dependent excitonic properties of twisted $MoSi_2N_4/WSi_2N_4$ heterostructure. The R type represents a small twist angle rotated from the AA stacking style. In the R type of twisted bilayers, three local stacking styles can be identified in Fig. 2, which have been denoted as AA, AB, and AC, respectively. In the AA configuration, two monolayers are aligned, and all atoms of the same type are superimposed. Based on the AA configuration, the AB and AC configurations are obtained by shifting the bottom WSi_2N_4 layer along the long-diagonal of the unit cell by 1/3 and 2/3, respectively. The interlayer distances and relative energies of the three heterostructures are given in Table I. Among the three configurations, AA possesses the largest interlayer distance (10.492 Å), and thus the weakest interlayer interaction. The largest interlayer distance is attributed to the repulsion arising from the N atoms superimposing in the two layers, leading to the highest relative energy. Meanwhile, AB and AC configurations share similar and lower interlayer distances and lower relative energies.

We first compare the quasiparticle band structure of

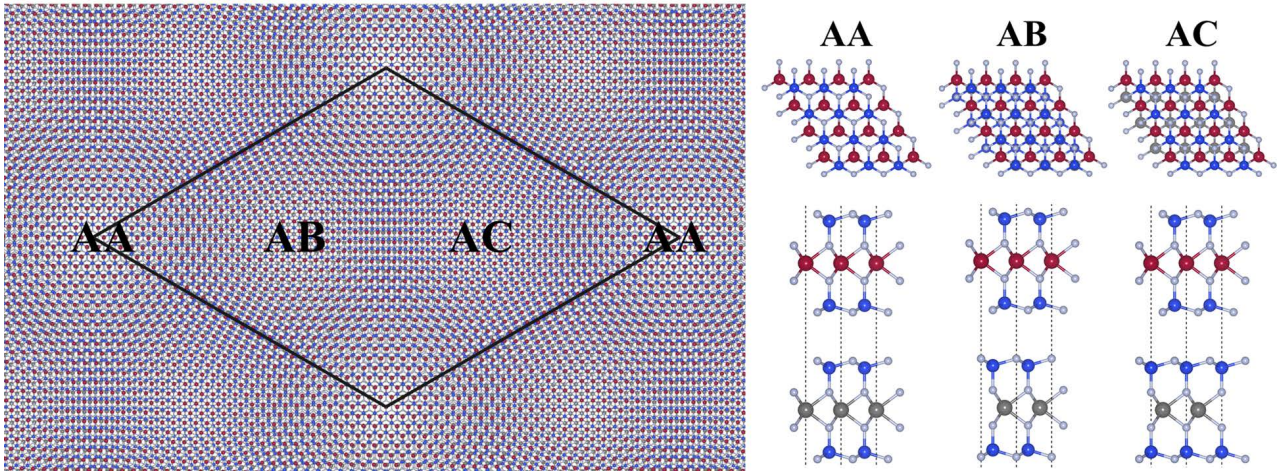

FIG. 2. The schematic plots of $MoSi_2N_4/WSi_2N_4$ heterostructure rotated from the AA stacking style with a small twist angle (moiré pattern). Three local stacking styles are identified and amplified with top and side views.

TABLE I. Interlayer distance d, relative energy ΔE, band gap, and energy and optical oscillator strength of the excitons for the three different $MoSi_2N_4/WSi_2N_4$ heterostructures.

							X_1		IX_0		X_2		X_3	
	d	ΔE	E_g^{DFT}	E_g^{GW}	E_{gKK}^{DFT}	E_{gKK}^{GW}	Energy	Osc. Str.	Energy	Osc. Str.	Energy	Osc. Str.	Energy	Osc. Str.
	(Å)	(meV)	(eV)	(eV)	(eV)	(eV)	(eV)	(a.u.)	(eV)	(a.u.)	(eV)	(a.u.)	(eV)	(a.u.)
AA	10.492	46	1.558	2.771	1.802	2.923	2.327	635	2.451	1.8×10^{-4}	2.757	593	2.864	1672
AB	10.144	0	1.454	2.652	1.706	2.891	2.298	652	2.505	3.1×10^{-4}	2.767	690	2.866	1014
AC	10.144	0	1.643	2.849	1.902	3.057	2.326	662	2.480	0.7×10^{-4}	2.720	562	2.847	1199

the three stacking styles. In AB and AC configurations, a typical type-II quasiparticle band alignment is obtained, which is similar to that of AA configuration in Fig. 1(a). We focus on the band gap at K point, because the vertical inter-band transitions and excitons around these points are responsible for optical spectra observed in the $MoSi_2N_4/WSi_2N_4$ moiré heterostructure. Table I summarizes the GW-calculated quasiparticle band gaps at the K point, which vary with the local stacking styles. For the R stacking styles, the energy variation is observable: AB style has the smallest band gap of 2.891 eV, while AC style possesses the largest band gap of 3.057 eV, showing a 166 meV variation of the quasiparticle band gap. This quasiparticle band gap variation is larger than that (100 meV) of R-type $MoSe_2/WSe_2$ twisted bilayers[38].

Figs. 3(a)-3(c) shows the optical absorption spectra of the three local stacking styles. Like many other 2D structures, enhanced excitonic effects are observed: after including e-h interactions, three excitonic peaks are formed below the quasiparticle band gap with significant e-h binding energies around a few hundred meV. Generally, there are two types of excitons, the intralayer (X_1, X_2, and X_3) and interlayer ones (IX_0). To elucidate these features, we break down each exciton state into its component transitions. The exciton wave function can be

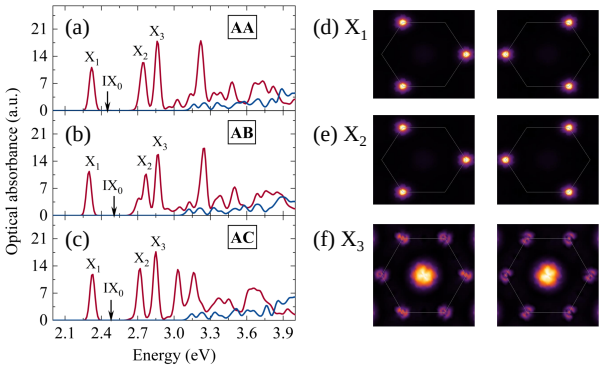

FIG. 3. (a)-(c)Optical absorption spectra of three identified local stacking styles in a $MoSi_2N_4/WSi_2N_4$ heterostructure with (red) and without e-h (blue) interactions. The energy of the interlayer exciton (IX_0) is marked by the black arrow. A 20-meV smearing to spectral widths is applied. (d)-(f)The reciprocal-space distribution of the charge density of bright exciton X_1, X_2, and X_3.

written as a linear combination of electron-hole pairs

$$\Psi_\lambda(r_e,r_h) = \sum_{vc\mathbf{k}} A^\lambda_{vc\mathbf{k}} \psi_{c\mathbf{k}}(r_e)\psi^*_{v\mathbf{k}}(r_h) \qquad (1)$$

where $\psi_{ck}(r_e)$ $(\psi^*_{vk}(r_h))$ is the quasi-particle electron

TABLE II. The character table of irreducible representations for the little group C_3 at K point, where I, C_3 and C_3^2 are three operation classes, A, E and E^* are the irreducible representations, and $w = e^{2\pi i/3}$.

	I	C_3	C_3^2	functions
A	1	1	1	z, x^2+y^2, z^2, J_z
E	1	w^2	w	$(x,y),(xz,yz),(x^2-y^2,xy),(J_x,J_y)$
E^*	1	w	w^2	

(hole) wavefunctions; λ indexes the exciton state; v and c index the occupied and unoccupied bands, respectively; and A^{λ}_{vck} is the electron-hole amplitude. The oscillator strengths f_S reads [26]

$$f_S = \frac{2|\mathbf{e}\cdot\langle 0|\mathbf{v}|S\rangle|^2}{\Omega^S}, \tag{2}$$

where the velocity matrix element is given by

$$\langle 0|\mathbf{v}|S\rangle = -i\Omega^S \sum_{vc\mathbf{k}} A^S_{vc\mathbf{k}} \langle v\mathbf{k}|\mathbf{r}|c\mathbf{k}\rangle. \tag{3}$$

There are three main bright exciton peaks X_1, X_2, and X_3 in the optical spectra below the quasiparticle direct gap. The exciton wavefunction shows that the first peak X_1 at lowest-energy (2.327 eV) arises from two degenerate excitonic states, and comes from transitions between VBM−1 and CBM (Table III) within $MoSi_2N_4$ monolayer, indicating the intralayer character. Fig. 3(d) shows the k-resolved e-h pair amplitudes for these two excitonic states of X_1, which are dominated by the e-h pairs near the minimum direct gap at K and K′ points, similar to that in monolayer MoS_2[39]. For the second peak X_2 around 2.757 eV, it comes from transitions between VBM and CBM+1 within WSi_2N_4 layer. The exciton X_2 originates from the direct transition at K point in reciprocal-space exciton wave function as shown in Fig. 3(e). At energies above the second peak, the third peak X_3 is due to the direct transition at Γ point partially coinciding with other direct transitions at K point, mostly within $MoSi_2N_4$ layer. The bright intralayer excitons have large dipole oscillator strength, because of the significant overlap of their electron and hole wave functions. In addition, the optical oscillator strengths of these three intralayer excitons (listed in Table I) are robust to the stacking style, having the same order of 10^2 for excitons X_1 and X_2, and the order of 10^3 for exciton X_3. This is very different from the excitons in TDMC moiré supercells, with the optical dipole oscillator strength modulated by a few orders of magnitude. These prominent optical oscillator strengths are meaningful for designing material platforms of moiré excitons and exciton condensations.

The interlayer exciton (IX_0) is marked by the black arrows in Figs. 3(a)-3(c). For AA stacking, the exciton IX_0 comes primarily from transitions between the VBM and CBM, which make up 99% of the exciton eigenvector. It is located at 2.451 eV, and the quasiparticle direct band gap is 2.923 eV, resulting in an e-h binding energy of 472 meV. This is similar to the binding energy (410 meV) of $MoSe_2/WSe_2$ bilayers[38]. The calculated optical oscillator strength of the interlayer exciton shows very small values (on the order of 10^{-6} times that of the intralayer exciton). We analyze the selection rule at K point to determine whether the very low brightness arises from the forbidden transition. The character table of the little group C_3 at K point is listed in Table II, and the calculated irreducible representations of energy bands at K point are labeled in Fig. 1(a). The selection rule at K point is determined by the nonzero matrix elements of the dipole operators[40], i.e., $\langle v\mathrm{K}|x|c\mathrm{K}\rangle$, $\langle v\mathrm{K}|y|c\mathrm{K}\rangle$ and $\langle v\mathrm{K}|z|c\mathrm{K}\rangle$. If these matrix elements of $\langle v\mathrm{K}|\mathbf{r}|c\mathrm{K}\rangle$ are zero, the forbidden transition will enable optically forbidden (dark) exciton, as indicated by Eqs. (2) and (3). Using the irreducible representations of energy bands at K point in Fig. 1(a), the character table in Table II and the orthogonality theorem, we obtain

$$\langle v\mathrm{K}|x|c\mathrm{K}\rangle \neq 0, \langle v\mathrm{K}|y|c\mathrm{K}\rangle \neq 0, \langle v\mathrm{K}|z|c\mathrm{K}\rangle = 0. \tag{4}$$

The allowed transitions in Eq. (4) with x-polarization or y-polarization exclude the possibility from the selection rule causing the very small optical oscillator strength of the interlayer exciton. We thus suggest that the enormous physical separation of electron and hole wave functions enable the quite small oscillator strength of the interlayer exciton. Note that here we still call the interlayer exciton IX_0 with such a negligible oscillator strength as dark exciton, since it is hardly directly accessible by optical techniques, as presented in Fig. 3.

As listed in Table I, the energy and brightness of the interlayer exciton are nearly independent of the stacking style. It is located at 2.451 eV in AA configuration, 2.505 in AB style, and 2.480 eV in AC style, and the corresponding exciton binding energies are 472, 386, and 577 meV, respectively. This dark interlayer exciton is very different from the stacking-dependent interlayer excitons in TMDCs, with dipole oscillator strength reaching the same order as those of intralayer excitons. Therefore, unlike in TMDCs [7], the moiré superlattice in bilayer $MoSi_2N_4/WSi_2N_4$ has minor influences on the interlayer excitonic properties. Unlike interlayer exciton with the lowest-energy in normal type-II heterostructures[3, 4], the interlayer exciton IX_0 in $MoSi_2N_4/WSi_2N_4$ type-II heterostructures has the energy higher than their intralayer exciton X_1, as shown in Fig. 3 and Table III. The intralayer exciton X_1 originating from the $MoSi_2N_4$ layer is located at around 2.3 eV, and it depends on the stacking order, with 0.1-0.2 eV below the interlayer exciton X_1. The binding energies of intralayer exciton X_1 are 791, 814, and 798 meV in AA, AB and AC stacking, respectively, which are 200-400 meV higher than the binding energy of the interlayer exciton. This is in stark contrast to the case of TMDC bilayers, in which the binding energy of intralayer and interlayer exciton differ by about 0.1 eV[31, 41]. The robust intralayer exciton and the atypical interlayer exciton in type-II $MoSi_2N_4/WSi_2N_4$

TABLE III. Dominant band-to-band transition and its weight $\sum_k |A_{vc\mathbf{k}}|^2$ of excitons in $MoSi_2N_4/WSi_2N_4$ heterostructures.

State	Conduction band	Valence band	$\sum_k \lvert A_{vc\mathbf{k}}\rvert^2$
IX_0	CBM	VBM	0.992
X_1	CBM	VBM-1	0.989
X_2	CBM+1	VBM	0.997
X_3	CBM	VBM-1	0.654

heterostructures enrich the new exciton mechanism in 2D materials and are beneficial for the design of moiré heterostructures and optoelectronic devices.

V. MACROSCOPIC DIELECTRIC MODEL FOR EXCITON SPECTRA IN $MOSI_2N_4/WSI_2N_4$ HETEROSTRUCTURE

To explain the atypical exciton spectra in $MoSi_2N_4/WSi_2N_4$ heterostructure, we build the following macroscopic dielectric model for 2D heterostructures. The monolayers at $z = 0$ and $z = d$ are assumed as an infinitely thin 2D dielectric slabs [42]. In this respect, assuming that the charge density at position $\mathbf{r}_\parallel$ inside the layer at $z = 0$ takes the form as $\rho(\mathbf{r}_\parallel, z) = e\delta(\mathbf{r}_\parallel)\delta(z)$, the induced potential $\phi(\mathbf{r}_\parallel, z)$ in real space follows the Poisson's equation:

$$\begin{aligned}\bigtriangledown^2\phi(\mathbf{r}_\parallel, z) = &-4\pi e\delta(\mathbf{r}_\parallel)\delta(z)\\ &-4\pi[\alpha_1\delta(z)+\alpha_2\delta(z-d)]\bigtriangledown_\parallel^2\phi(\mathbf{r}_\parallel, z),\end{aligned} \tag{5}$$

where the second term arises from the 2D macroscopic polarization with α_1 and α_2 as the 2D polarizabilities for the monolayers at $z = 0$ and $z = d$, respectively. After performing the following Fourier transform,

$$\phi(\mathbf{r}_\parallel, z) = \sum_{\mathbf{q},G_\perp}\phi(\mathbf{q}, G_\perp)e^{i\mathbf{q}\cdot\mathbf{r}_\parallel}e^{iG_\perp z}, \tag{6}$$

where $\mathbf{q}$ and $G_\perp$ are the in-plane and out-of-plane components of the wave vector, respectively, we rewrite Eq. (5) as

$$\sum_{G_\perp}(|\mathbf{q}|^2+{G_\perp}^2)\phi(\mathbf{q}, G_\perp)e^{iG_\perp z} = \sum_{G_\perp}\left[4\pi e-4\pi(\alpha_1+e^{-iG_\perp d}\alpha_2)|\mathbf{q}|^2\frac{1}{2\pi}\sum_{G'_\perp}\phi(\mathbf{q}, G'_\perp)e^{iG'_\perp z}\right]e^{iG_\perp z}, \tag{7}$$

where d is the distance between the two monolayers. Simplifying Eq. (7), we write $\phi(\mathbf{q}, G_\perp)$ as

$$\phi(\mathbf{q}, G_\perp) = \frac{4\pi e-4\pi(\alpha_1+e^{-iG_\perp d}\alpha_2)|\mathbf{q}|^2\phi_{2D}(\mathbf{q}, z)}{|\mathbf{q}|^2+{G_\perp}^2}, \tag{8}$$

where

$$\phi_{2D}(\mathbf{q}, z) = \frac{1}{2\pi}\sum_{G_\perp}\phi(\mathbf{q}, G_\perp)e^{iG_\perp z} \tag{9}$$

Performing a sum over $G_\perp$ for Eq. (8) and using Eq. (9), we have

$$\phi_{2D}(\mathbf{q}, z) = \frac{4\pi e-4\pi|\mathbf{q}|^2\alpha_1\phi_{2D}(\mathbf{q}, z)}{2\pi}\sum_{G_\perp}\frac{e^{iG_\perp z}}{|\mathbf{q}|^2+{G_\perp}^2}-\frac{4\pi|\mathbf{q}|^2\alpha_2\phi_{2D}(\mathbf{q}, z)}{2\pi}\sum_{G_\perp}\frac{e^{iG_\perp(z-d)}}{|\mathbf{q}|^2+{G_\perp}^2}. \tag{10}$$

Then we obtain $\phi_{2D}(\mathbf{q}, z)$ as

$$\phi_{2D}(\mathbf{q}, z) = \frac{2\pi e e^{-|\mathbf{q}||z|}}{|\mathbf{q}|+2\pi|\mathbf{q}|^2\alpha_1 e^{-|\mathbf{q}||z|}+2\pi|\mathbf{q}|^2\alpha_2 e^{-|\mathbf{q}||z-d|}}. \tag{11}$$

Consequently, the induced intralayer potential and interlayer potential correspondingly read

$$\phi_{intra}(\mathbf{q}) = \frac{2\pi e}{|\mathbf{q}|+2\pi|\mathbf{q}|^2\alpha_1+2\pi|\mathbf{q}|^2\alpha_2 e^{-|\mathbf{q}|d}}, \tag{12}$$

i.e., $\phi_{2D}(\mathbf{q}, z = 0)$, and

$$\phi_{inter}(\mathbf{q}) = \frac{2\pi e e^{-|\mathbf{q}|d}}{|\mathbf{q}|+2\pi|\mathbf{q}|^2\alpha_1 e^{-|\mathbf{q}|d}+2\pi|\mathbf{q}|^2\alpha_2}, \tag{13}$$

i.e., $\phi_{2D}(\mathbf{q}, z = d)$. By comparison, for 2D monolayer materials with the polarizability α and $d = 0$ in Eq. (11), the induced potential reads

$$\phi_{mono}(\mathbf{q}) = \frac{2\pi e}{|\mathbf{q}|+2\pi|\mathbf{q}|^2\alpha}, \tag{14}$$

which reproduces the result in Ref. [42].

Eqs. (12)-(14) indicate that the three potentials decay with the increasing of $|\mathbf{q}|$ and diverge at $|\mathbf{q}| = 0$. From $\phi_\eta(\mathbf{q}) = \frac{2\pi e}{\tilde{\epsilon}_\eta(\mathbf{q})|\mathbf{q}|}$, we define the $\mathbf{q}$-dependent effective dielectric function $\tilde{\epsilon}_\eta(\mathbf{q})$ as

$$\tilde{\epsilon}_\eta(\mathbf{q}) = \frac{2\pi e}{\phi_\eta(\mathbf{q})|\mathbf{q}|}, \tag{15}$$

where $\eta = \{intra, inter, mono\}$ is the exciton type. The Coulomb interaction in Eqs. (12)-(13) with a corresponding cutoff $1/a_B^\eta$ of $|\mathbf{q}|$ is an estimation of the exciton binding energy E_b^η in SI unit, i.e.,

$$E_b^\eta = \frac{1}{4\pi\epsilon_0 S}\int_0^{2\pi} d\theta \int_0^{1/a_B^\eta} e\phi_\eta(q) q dq = \frac{\pi e^2}{\epsilon_0 S}\int_0^{1/a_B^\eta} \frac{1}{\tilde{\epsilon}_\eta(q)} dq, \tag{16}$$

where $q = |\mathbf{q}|$, e is the unit charge, S is the area, ϵ_0 is the vacuum dielectric constant, a_B^η is the η-exciton Bohr radius as the root mean square radius of the exciton wave function in real space. Based on the fact that the terms with the rapid decaying factor $e^{-|\mathbf{q}|d}$ in the denominators of Eqs. (12) and (13) are small correction terms, we neglect them and derive the following analytically approximate expressions of E_b^{intra} and E_b^{inter},

$$\begin{aligned} E_b^{intra} &= \frac{e^2}{2\epsilon_0 S\alpha_1}\ln\left(1 + \frac{2\pi\alpha_1}{a_B^{intra}}\right), \\ E_b^{inter} &= \frac{e^2 e^{\frac{d}{2\pi\alpha_2}}}{2\epsilon_0 S\alpha_2}\left[\mathrm{Ei}(-\frac{d}{a_B^{inter}} - \frac{d}{2\pi\alpha_2}) - \mathrm{Ei}(-\frac{d}{2\pi\alpha_2})\right], \end{aligned} \tag{17}$$

where $\mathrm{Ei}(x)$ is the special function giving the exponential integral function $\mathrm{Ei}(x) = \int_{-\infty}^{x}\frac{e^t}{t}dt$. Eqs. (11)-(13), Eq. (16) and Eq. (17) are the central results of the macroscopic dielectric model for excitons in bilayer systems.

In the above macroscopic model, the effective dielectric function $\tilde{\epsilon}_\eta(\mathbf{q}) = 2\pi e/(\phi_\eta(\mathbf{q}))|\mathbf{q}|$ is determined by the three parameters α_1, α_2 and d. We have calculated their values from the ab initio method and list them in Table IV. The polarizabilities α_1 and α_2 are close to each other for $MoSi_2N_4/WSi_2N_4$ and MoS_2/WS_2 with their values near 6 Å. However, the layer distance $d = 6.3$ Å for MoS_2/WS_2 is almost half of that for $MoSi_2N_4/WSi_2N_4$ with it values 10.492 Å. We extract the Bohr radius a_B^η for the η exciton from the distribution of exciton wave function given by the GW-BSE calculations. As listed in Table IV, excitons in $MoSi_2N_4/WSi_2N_4$ have their Bohr radii $a_B^{intra} \sim 7.142$ Å and $a_B^{inter} \sim 9.091$ Å, and excitons in MoS_2/WS_2 have their Bohr radii $a_B^{intra} \sim 11.120$ Å and $a_B^{inter} \sim 15.384$ Å. The areas S calculated by using Eq. (14), Eq. (16), $E_b^{mono} \sim 0.95$ eV and $a_B^{mono} \sim 5.926$ Å for $MoSi_2N_4$, and $E_b^{mono} \sim 0.5$ eV and $a_B^{mono} \sim 12.7$ Å for MoS_2 from GW computations are about 31.69 $Å^2$ and 40.06 $Å^2$, respectively.

Fig. 4(a) shows the q-dependent binding energy densities $\frac{\pi e^2}{\epsilon_0 S}\frac{1}{\tilde{\epsilon}_\eta(q)}$ of exciton in Eq. (16) for the intralayer exciton X_1 and the interlayer exciton IX_0 in $MoSi_2N_4/WSi_2N_4$ heterostructure as well as the exciton binding energy density for $MoSi_2N_4$ monolayer. For comparisons, Fig. 4(b) shows the corresponding exciton binding energy densities for MoS_2/WS_2 heterostructure and MoS_2 monolayer. The sharper decay of binding energy density for interlayer excitons than that for intralayer excitons exists for both $MoSi_2N_4/WSi_2N_4$ and MoS_2/WS_2 heterostructures in Fig. 4(a) and 4(b), because of the additional factor $e^{-|\mathbf{q}|d}$ in the numerator for interlayer excitons in Eq. (13). Therefore, the binding energy density of intralayer excitons is always larger than that of the interlayer excitons. From Eq. (16), the exciton binding energy is determined by the area under the curve from 0 to $(a_B^\eta)^{-1}$. Consequently, the less Bohr radius for intralayer excitons results in a larger binding energy than that for interlayer excitons. The calculated binding energy are $E_b^{inter} \sim 0.428$ eV and $E_b^{intra} \sim 0.692$ eV for $MoSi_2N_4/WSi_2N_4$ heterostructure, and the calculated binding energy $E_b^{inter} \sim 0.294$ eV and $E_b^{intra} = 0.397$ eV for MoS_2/WS_2 heterostructure, as shown in Table IV. These results from the macroscopic model are comparable with those from the GW-BSE approach. We figure out that the macroscopic model only includes the direct interaction term without the exchange interaction contribution. The GW-BSE calculation results show that the exchange energy for both interlayer and intralayer excitons is relatively small comparing with the direct term in $MoSi_2N_4/WSi_2N_4$ heterostructures. The discrepancy between the classical electrostatic binding energy and the GW-BSE value especially for the intralayer exciton with a difference of 200 meV arises from Eq. (16), which is only an estimation of the exciton binding energy. The more accurate value is given by the GW-BSE.

Another difference for their binding energy between $MoSi_2N_4/WSi_2N_4$ and MoS_2/WS_2 heterostructures is that the difference $E_b^{intra} - E_b^{inter}$ for $MoSi_2N_4/WSi_2N_4$ is larger than that for MoS_2/WS_2, as shown in Table IV. Actually, we can also clearly see the larger binding energy density difference for $MoSi_2N_4/WSi_2N_4$ in Fig. 4(a)

TABLE IV. The 2D polarizability α_1 ($MoSi_2N_4$ or MoS_2), α_2 (WSi_2N_4 or WS_2), layer distance d, exciton Bohr radius a_B, and exciton binding energy calculated by our model(E_b^{Model}) and GW+BSE (E_b^{BSE}) for $MoSi_2N_4/WSi_2N_4$ and MoS_2/WS_2 heterostructures.

						inter		intra	
	α_1(Å)	α_2(Å)	d(Å)	a_B^{inter}(Å)	a_B^{intra}(Å)	$E_b^{Model}(eV)$	E_b^{BSE}(eV)	$E_b^{Model}(eV)$	E_b^{BSE}(eV)
$MoSi_2N_4/WSi_2N_4$	5.926	5.615	10.492	9.091	7.142	0.428	0.472	0.692	0.903
MoS_2/WS_2	6.489	6.311	6.300	15.384	11.120	0.294	0.430	0.397	0.500

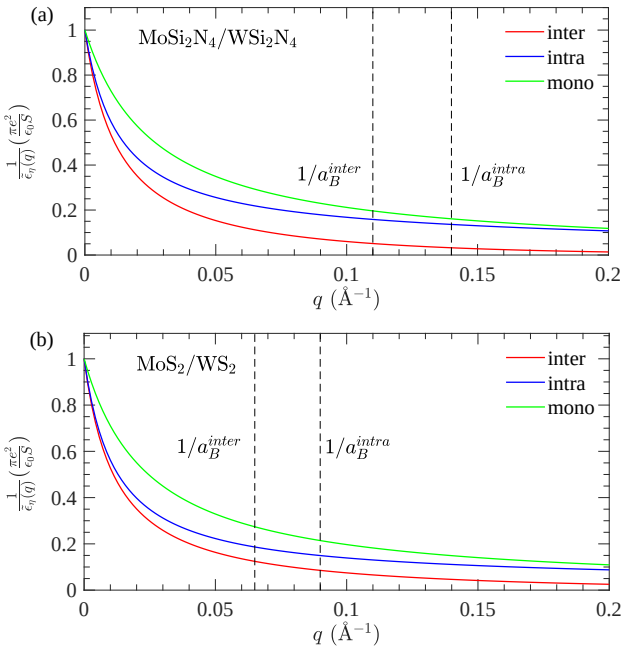

FIG. 4. q-dependent binding energy densities for η-exciton in Eq. (16) for (a) $MoSi_2N_4/WSi_2N_4$ and (b) MoS_2/WS_2 heterostructures, where $\eta =$ inter, intra or mono denote the interlayer, intralayer or monolayer excitons, and a_B^{inter} and a_B^{intra} are the Bohr radii for the interlayer and intralayer excitons, respectively.

than that for MoS_2/WS_2 in Fig. 4(b), as a result of the larger layer distance d leading to the sharper decay for $MoSi_2N_4/WSi_2N_4$. Because the energy position E_p^η of exciton absorption peak is determined by the difference between the band edge E_{be}^η and the binding energy E_b^η for η-exciton, i.e., $E_p^\eta = E_{be}^\eta - E_b^\eta$, the larger binding energy difference between E_b^{intra} and E_b^{inter} with similar band edges $E_{be}^{intra} \sim E_{be}^{inter}$ induce the atypical exciton spectra, i.e., $E_p^{inter} > E_p^{intra}$, for $MoSi_2N_4/WSi_2N_4$, comparing with that for MoS_2/WS_2. Therefore, our macroscopic model indicates that the atypical exciton spectra in $MoSi_2N_4/WSi_2N_4$ is mainly attributed to its larger layer distance and its smaller exciton Bohr radius comparing with MoS_2/WS_2.

VI. CONCLUSION

In conclusion, we systematically study the band alignment and excitons in $MoSi_2N_4/WSi_2N_4$ heterostructure using ab initio GW and Bethe-Salpeter equation calculations. The quasiparticle band alignment is type II and insensitive to the dielectric environment screening, with band edge energies of composed single layer changing about 0.15 eV, leading to a 4% reduction in the quasiparticle band gap compared to free-standing monolayers. However, unlike normal type-II heterostructures, optically, $MoSi_2N_4/WSi_2N_4$ heterostructure behaves like a type-I heterostructure, where the lowest optical excitations is intralayer exciton while the interlayer exciton is higher in energy. Using a macroscopic dielectric model, we attribute this unique feature to the large layer distance and small exciton Bohr radius of $MoSi_2N_4/WSi_2N_4$ heterostructure. Additionally, we find the interlayer exciton is dark due to negligible electron-hole overlap, and the energy and oscillator strength of intralayer exciton are almost independent of the stacking configuration. The atypical interlayer exciton and robust intralayer exciton in type-II $MoSi_2N_4/WSi_2N_4$ heterostructures enrich the picture of excitons in 2D materials and are useful for the design of moiré heterostructures and optoelectronic devices.

ACKNOWLEDGEMENT

H.Z. acknowledges support from the National Natural Science Foundation of China (Grant Nos. 12104421 and 11947218), Y.W. acknowledges support from the NSFC (Grant No. 12247101), the 111 Project (Grant No. B20063), and the National Key Research and Development Program of China (Grant No. 2022YFA1402704). This work is also supported by Zhejiang Provincial Natural Science Foundation of China (Grant No. LY23A040005), the "CUG Scholar" Scientific Research Funds at China University of Geosciences (Wuhan) (Project No. 2021032), and the Fundamental Research Funds for the Central Universities, China University of Geosciences (Wuhan) (Grant No. G1323523065). S.G. is supported as part of the Institute for Quantum Matter, an Energy Frontier Research Center funded by the U.S. Department of Energy, Office of Science, Basic Energy Sciences under Award No. DE-SC0019331. Numerical

calculations presented in this paper have been performed on a supercomputing system in the Supercomputing Center of Wuhan University.

[1] F. Wang, T. Heinz, E. Jin, O. K. Ma, and R. EC, Nat. Nanotechnol. **13**, 994 (2018).
[2] M. Fogler, L. Butov, and K. Novoselov, Nat. Commun. **5**, 4555 (2014).
[3] K. F. Mak and J. Shan, Nat. Nanotechnol. **13**, 974 (2018).
[4] J. Choi, M. Florian, A. Steinhoff, D. Erben, K. Tran, D. S. Kim, L. Sun, J. Quan, R. Claassen, S. Majumder, *et al.*, Phys. Rev. Lett. **126**, 047401 (2021).
[5] H. Ochoa, Phys. Rev. B **100**, 155426 (2019).
[6] D. M. Kennes, M. Claassen, L. Xian, A. Georges, A. J. Millis, J. Hone, C. R. Dean, D. Basov, A. N. Pasupathy, and A. Rubio, Nat. Phys. **17**, 155 (2021).
[7] H. Yu, G.-B. Liu, J. Tang, X. Xu, and W. Yao, Sci. Adv. **3**, e1701696 (2017).
[8] K. Tran, G. Moody, F. Wu, X. Lu, J. Choi, K. Kim, A. Rai, D. A. Sanchez, J. Quan, A. Singh, *et al.*, Nature **567**, 71 (2019).
[9] Y.-L. Hong, Z. Liu, L. Wang, T. Zhou, W. Ma, C. Xu, S. Feng, L. Chen, M.-L. Chen, D.-M. Sun, *et al.*, Science **369**, 670 (2020).
[10] C. Yang, Z. Song, X. Sun, and J. Lu, Phys. Rev. B **103**, 035308 (2021).
[11] S. Li, W. Wu, X. Feng, S. Guan, W. Feng, Y. Yao, and S. A. Yang, Phys. Rev. B **102**, 235435 (2020).
[12] Q. Cui, Y. Zhu, J. Liang, P. Cui, and H. Yang, Phys. Rev. B **103**, 085421 (2021).
[13] B. Mortazavi, B. Javvaji, F. Shojaei, T. Rabczuk, A. V. Shapeev, and X. Zhuang, Nano Energy **82**, 105716 (2021).
[14] S.-D. Guo, Y.-T. Zhu, W.-Q. Mu, and W.-C. Ren, EPL **132**, 57002 (2020).
[15] D. Liang, S. Xu, P. Lu, and Y. Cai, Phys. Rev. B **105**, 195302 (2022).
[16] Y. Wu, Z. Tang, W. Xia, W. Gao, F. Jia, Y. Zhang, W. Zhu, W. Zhang, and P. Zhang, NPJ Comput. Mater. **8**, 1 (2022).
[17] J. P. Perdew, K. Burke, and M. Ernzerhof, Phys. Rev. Lett. **77**, 3865 (1996).
[18] P. Giannozzi, S. Baroni, N. Bonini, M. Calandra, R. Car, C. Cavazzoni, D. Ceresoli, G. L. Chiarotti, M. Cococcioni, I. Dabo, *et al.*, J. Phys. Condens. Matter **21**, 395502 (2009).
[19] A. Otero-De-La-Roza and E. R. Johnson, J. Chem. Phys. **136**, 174109 (2012).
[20] N. Troullier and J. L. Martins, Phys. Rev. B **43**, 1993 (1991).
[21] Z. Wang, X. Kuang, G. Yu, P. Zhao, H. Zhong, and S. Yuan, Phys. Rev. B **104**, 155110 (2021).
[22] M. S. Hybertsen and S. G. Louie, Phys. Rev. B **34**, 5390 (1986).
[23] D. Y. Qiu, F. H. Da Jornada, and S. G. Louie, Physical Review B **93**, 235435 (2016).
[24] F. H. da Jornada, D. Y. Qiu, and S. G. Louie, Physical Review B **95**, 035109 (2017).
[25] M. Rohlfing and S. G. Louie, Phys. Rev. B **62**, 4927 (2000).
[26] J. Deslippe, G. Samsonidze, D. A. Strubbe, M. Jain, M. L. Cohen, and S. G. Louie, Comput. Phys. Commun. **183**, 1269 (2012).
[27] S. Ismail-Beigi, Phys. Rev. B **73**, 233103 (2006).
[28] C. A. Rozzi, D. Varsano, A. Marini, E. K. U. Gross, and A. Rubio, Phys. Rev. B **73**, 205119 (2006).
[29] C. D. Spataru, S. Ismail-Beigi, L. X. Benedict, and S. G. Louie, Appl. Phys. A: Mater. Sci. Process. **78**, 1129 (2004).
[30] L. Yang, C. D. Spataru, S. G. Louie, and M. Y. Chou, Phys. Rev. B **75**, 201304(R) (2007).
[31] S. Gao, L. Yang, and C. D. Spataru, Nano Lett. **17**, 7809 (2017).
[32] J. He, K. Hummer, and C. Franchini, Phys. Rev. B **89**, 075409 (2014).
[33] H. Zhong, W. Xiong, P. Lv, J. Yu, and S. Yuan, Phys. Rev. B **103**, 085124 (2021).
[34] Y. Zhang, T.-R. Chang, B. Zhou, Y.-T. Cui, H. Yan, Z. Liu, F. Schmitt, J. Lee, R. Moore, Y. Chen, *et al.*, Nat. Nanotechnol. **9**, 111 (2014).
[35] M. M. Ugeda, A. J. Bradley, S.-F. Shi, F. H. Da Jornada, Y. Zhang, D. Y. Qiu, W. Ruan, S.-K. Mo, Z. Hussain, Z.-X. Shen, *et al.*, Nat. Mater. **13**, 1091 (2014).
[36] D. Y. Qiu, F. H. da Jornada, and S. G. Louie, Nano Lett. **17**, 4706 (2017).
[37] S. Yin, Q. Luo, D. Wei, G. Guo, X. Sun, Y. Tang, and X. Dai, Results Phys. **33**, 105172 (2022).
[38] X. Lu, X. Li, and L. Yang, Phys. Rev. B **100**, 155416 (2019).
[39] D. Y. Qiu, F. H. da Jornada, and S. G. Louie, Phys. Rev. Lett. **111**, 216805 (2013).
[40] Y. Wang, G. Yu, M. Rösner, M. I. Katsnelson, H.-Q. Lin, and S. Yuan, Phys. Rev. X **12**, 021055 (2022).
[41] E. Torun, H. P. C. Miranda, A. Molina-Sánchez, and L. Wirtz, Phys. Rev. B **97**, 245427 (2018).
[42] P. Cudazzo, I. V. Tokatly, and A. Rubio, Phys. Rev. B **84**, 085406 (2011).